Molecular Dynamics Studies of Stress−Strain Behavior of Silica Glass under a Tensile Load

Alfonso Pedone,[†] Gianluca Malavasi,[†] M. Cristina Menziani,*[,†] Ulderico Segre,[†] and Alastair N. Cormack[‡]

Dipartimento di Chimica, Università di Modena e Reggio Emilia, Via G. Campi 183, 41100 Modena, Italy, and Kazuo Inamori School of Engineering, New York State College of Ceramics, Alfred University, Alfred, New York 14802

Received February 11, 2008

Molecular dynamics (MD) simulations were carried out to study the stress−strain diagrams of crystalline and amorphous silica under different nonequilibrium conditions. The responses of a tensile load were recorded in two cases. In one case, the system was not allowed to relax along the transverse direction (null Poisson's ratio), while in the other case, the deformations were allowed in directions perpendicular to the strained one. The higher strength of crystalline silica as compared to amorphous silica resulted from a different distribution of ring sizes. The results obtained for the inert failure strains and intrinsic strength of the silica glass were in good agreement with the experimental data, and the nonlinear elastic behavior of the glass was reproduced along with the effects of strain rate and temperature variation. Elastic properties extracted from stress−strain diagrams also were compared with the properties calculated by means of static methods and with experimental data.

1. Introduction

Mechanical properties and fracture mechanisms of silicate glasses are of fundamental importance in designing materials to comply with specific technological applications. Glasses and ceramics are considered to be brittle materials because they fracture without any appreciable deformation and by rapid crack propagation with a direction very nearly perpendicular to the direction of applied tensile stress, producing a relatively flat surface.[1,2] The problem of prediction of the initiation of brittle fracture and calculation of the energetics of the process was first addressed in a pioneering work by Griffith,[3] then improved by Irwin[4] and Barenblatt[5] on the basis of continuum mechanics.

The measured fracture strengths for most brittle materials are significantly lower than those predicted by theoretical calculations based on atomic bonding energies.[6] This discrepancy is explained by the presence of very small, microscopic flaws or cracks that always exist under normal conditions at the surface and within the interior of a material. However, neither the path of the crack, nor its propagation characteristics, nor the structure of the freshly formed surfaces were addressed until atomic dynamics in high stress regions became feasible. In the past decade, with the advent of powerful computers and development of efficient algorithms to implement atomistic computational techniques such as molecular dynamics (MD), computer experiments were carried out extensively to study fracture mechanisms.[6–21]

Experimental studies of brittle fracture in glasses have shown that fracture processes may be separated into sudden fracture and slow crack growth. In the latter, the environment, especially water, is allowed to interact with strained bonds at the tip of existing cracks and can induce physisorption and chemisorption processes that weaken the bond and allow the crack to advance slowly.[22] Ab initio[23] and semiempirical molecular orbital[24] studies have addressed the problem of strain induced chemisorption processes at the crack tip, which

* Corresponding author. E-mail: menziani@unimore.it.
[†] Università di Modena e Reggio Emilia.
[‡] Alfred University.

(1) Lawn, B. *Fracture of Brittle Solids*; Cambridge University Press: Cambridge, 1993.
(2) Callister, W. D. *Materials Science and Engineering: An Introduction*, 7th ed.; John Wiley and Sons: New York, 2007.
(3) Griffith, A. A. *Philos. Trans. R. Soc. London, Ser. A* **1921**, *221*, 163.
(4) Irwin, D. R. *J. Appl. Mech.* **1957**, *24*, 361.
(5) Barenblatt, G. I. *Adv. Appl. Mech.* **1962**, *7*, 55.
(6) Swiler, T. P.; Simmons, J. H.; Wright, A. C. *J. Non-Cryst. Solids* **1995**, *182*, 68.
(7) Soules, T. F.; Busbey, R. F. *J. Chem. Phys.* **1983**, *78*, 6307.
(8) Kieffer, J.; Angell, C. A. *J. Non-Cryst. Solids* **1988**, *106*, 336.
(9) Ochoa, R.; Simmons, J. H. *J. Non-Cryst. Solids* **1985**, *75*, 413.
(10) Ochoa, R.; Swiler, T. P.; Simmons, J. H. *J. Non-Cryst. Solids* **1991**, *128*, 57.
(11) Simmons, J. H.; Swiler, T. P.; Ochoa, R. *J. Non-Cryst. Solids* **1991**, *134*, 179.
(12) Swiler, T. P.; Varghese, T.; Simmons, J. H. *J. Non-Cryst. Solids* **1995**, *181*, 238.
(13) Abraham, F. F.; Brodbeck, D.; Rafey, R. A.; Rudge, W. E. *Phys. Rev. Lett.* **1994**, *73*, 272.
(14) Campbell, T.; Kalia, R. K.; Nakano, A.; Shimojo, F.; Tsuruta, K.; Vashishta, P. *Phys. Rev. Lett.* **1999**, *82*, 4018.
(15) Muralidharan, K.; Simmons, J. H.; Deymier, P. A.; Runge, K. *J. Non-Cryst. Solids* **2005**, *351*, 1532.
(16) Nakano, A.; Kalia, R. K.; Vashishta, P. *Phys. Rev. Lett.* **1994**, *73*, 2336.
(17) Nakano, A.; Kalia, R. K.; Vashishta, P. *Phys. Rev. Lett.* **1995**, *75*, 3138.
(18) Rountree, C. L.; Kalia, R. K.; Lidorikis, E.; Nakano, A.; Van Brutzel, L.; Vashishta, P. *Annu. Rev. Mater. Res.* **2002**, *32*, 377.
(19) Van Brutzel, L.; Rountree, C. L.; Kalia, R. K.; Nakano, A.; Vashishta, P. *Res. Soc. Symp. Proc.* **2002**, *703*, 117.
(20) Li, Q.-K.; Li, M. *Appl. Phys. Lett.* **2005**, *87*, 31910.
(21) Li, Q.-K.; Li, M. *Intermetallics* **2006**, *14*, 1005.
(22) Mihalske, T. A.; Frieman, S. W. *J. Am. Ceram. Soc.* **1984**, *66*, 407.
(23) West, J. K.; Hench, L. L. *J. Mater. Sci.* **1994**, *29*, 3601.

10.1021/cm800413v CCC: $40.75
Published on Web 06/11/2008

control the slow crack growth phenomenon. Conversely, in the rapid crack growth process, the crack is assumed to propagate with no interaction with the environment. The MD method is based on the calculation of particle motions, and therefore, it is well-suited to describe the dynamics of crack growth. However, because of the use of classical interatomic potentials, it does not provide a good basis for studying chemical reactions. Therefore, it is more suited to model the rapid crack growth than the slow crack process.

Soules and Busbey[7] first reported studies of sodium silicate glass under both tension and compression conditions. They used systems of ∼1000−2000 atoms with free surfaces subjected to both uniaxial and biaxial expansions. In the case of uniaxial strain, the strain was applied by displacing the atoms close to the surface; atomic bonds were first elastically stretched, and then a considerable plastic deformation was found. A flaw was then formed that led to separation. The stress−strain diagrams evidenced brittle fracture since the tensile stress dropped rapidly after reaching the maximum stress point. Kieffer and Angell[8]simulated rupture of the silica glass structure by isotropic expansion through the application of a negative pressure. After opening the bond angles, the structure catastrophically fractured by developing a self-similar void structure that was described by a fractal dimension changing linearly with density.

Simmons et al.[6,9−12,15] examined the fracture process of vitreous silica and α-cristobalite in a systematic way. They applied a uniaxial strain at different strain rates (5×10^9 to 1×10^{11} s^{-1}) to glass samples of 3000 atoms and analyzed the effect of strain rates on the stress−strain curves. The application of the uniaxial strain was uniform throughout the sample. Periodic boundary conditions were applied along three directions, but they did not allow the system to relax along the transverse directions leading to a null Poisson's ratio ($\nu = 0$). They observed that the strength of the glass increased with increasing strain rates. This was attributed to the fact that at lower strain rates, the sample has more time to relieve its strain by structural rearrangement of atoms. Four distinct regions were identified: (a) the elastic regime, where stress increased linearly with strain, (b) a yield region, where stress varied very slowly with strain, (c) a region where there was a dramatic drop in the stress with increasing strain, and finally (d) separation of the sample corresponding to zero stress. The fracture was observed to consist of growth and coalescence of preexisting voids in the structure. At low strain rates, the strain added uniformly to the structure is allowed to flow from higher density regions to lower ones, leading to the coalescence of voids. They estimated the critical void to be 4−4.5 Å in radius, depending on the strain rate. Performing the same simulations with different potential models, they found different values for intrinsic strength and Young's modulus, but no difference was observed in the behavior of the strained glass samples. They concluded that the fracture controlling the processes was potential independent.

Van Brutzel et al.[19] studied the propagation of a crack in silica glass by using multimillion atom simulations and the potential developed by Vashishta et al.[25] They created a V-shaped notch on one edge of the simulation box and subjected the box to an external strain by displacing atoms in the top and bottom layers. They observed the growth and coalescence of voids and pores with a radius of 50−60 Å near the crack tip. The effect of the temperature also was studied, and it was found that at high temperatures, some voids grew in regions further away from the crack tip, leading to secondary crack growth. Nakano et al.[17] also performed multimillion atom simulations to study the dynamics and morphology of brittle cracks of amorphous silicon nitride films, observing a similar fracture mechanism. In almost all the works mentioned previously, a common finding is the formation and coalescence of voids and pores that lead to the brittle failure of strained glasses.

However, despite intense investigation, the fracture mechanism of brittle glasses is still controversial. An issue of current interest is the possibility of plastic deformation at crack tips in silicate glasses at room temperature. A recent AFM study on silicate glasses undergoing fracture reported the formation of plastic zones on the nanometer scale (cavities 20 nm long and 5 nm deep).[26] However, a subsequent study of silicate glasses under similar conditions did not produce such cavities.[27]

In this paper, a detailed study of the effects of (a) relaxation of box sides perpendicular to the strained direction ($\nu \neq 0$), (b) temperature, (c) strain rate, and (d) starting structure on the stress−strain diagrams of crystalline and amorphous silica was performed to clarify the behavior of stress−strain diagrams and the fracture mechanism under different conditions. The analysis will be limited to flaw-free and nonchemically mediated fractures.

2. Computational Procedures

A great benefit of MD simulations is that different systems may be modeled with fully identical characteristics, except for the starting structure. Therefore, we modeled both silica glass and silica crystal, with the same force field. The silica crystal was chosen to be β-cristobalite because it has a cubic symmetry with the same mechanical properties along the three directions [100], [010], and [001], a density of 2.19 g/cm^3, and a structure composed of six-membered rings that makes it most similar to the glass short-range structure. Consequently, a comparison between glass and crystal behavior only reflects the effect of order versus disorder on the fracture process. Systems of 12 288 atoms of silica glass and β-cristobalite were modeled using pairwise empirical potentials developed by Pedone et al.,[28] which have been demonstrated to reproduce both structural and elastic properties of a wide range of silicate crystals and glasses.[28,29]

A practical aspect of the simulation of β-cristobalite has to be mentioned. In nature, β-cristobalite is a high temperature polymorph and inverts to the α-form at low temperatures. For comparison with glass, the simulation procedure requires that the (experimental)

(24) Zhu, T.; Li, J.; Yip, S.; Barlett, R. J.; Trickey, S. B.; de Leeuw, N. H. *Mol. Simul.* **2003**, *29*, 671.

(25) Vashishta, P.; Kalia, R. K.; Rino, J. P.; Ebbsjo, I. *Phys. Rev. B: Condens. Matter Mater. Phys.* **1990**, *41*, 12197.

(26) Célarié, F.; Prades, S.; Bonanomy, D.; Ferrero, L.; Bouchaud, E.; Guillot, C.; Marlière, C. *Phys. Rev. Lett.* **2003**, *90*, 75504.

(27) Guin, J.-P.; Wiederhorn, S. M. *Phys. Rev. Lett.* **2004**, *92*, 215502.

(28) Pedone, A.; Malavasi, G.; Menziani, M. C.; Cormack, A. N.; Segre, U. *J. Phys. Chem. B* **2006**, *110*, 11780.

(29) Pedone, A.; Malavasi, G.; Cormack, A. N.; Segre, U.; Menziani, M. C. *Chem. Mater.* **2007**, *19* (13), 3144.

β-cristobalite structure be relaxed to zero stress at 300 K before the tensile load is applied. The relaxation leads to a final density of 2.22 g/cm^3 and a thermally disordered structure due to a contraction of 30° of the Si−O−Si angles, which are 180° in the β-cristobalite structure. Thus, the simulated β-cristobalite structure tends to assume the α-form, as expected, but the cubic periodic boundary conditions, which were retained, do not allow complete conversion. However, since we want to study the effect of the different ring size distribution of the crystal with respect to the one of the silica glass and since the ring size distribution of β-cristobalite does not change after relaxation at room temperature, this starting point is still acceptable. We call this α-form constrained in the cubic cell amorphous-cristobalite hereafter.

Silica glass was obtained by a melt−quench process of the experimental β-cristobalite. The system was heated at 6000 K, a temperature more than adequate to bring it to the liquid state in the framework of the adopted force field. The melt was then equilibrated for 100 ps and subsequently cooled continuously from 6000 to 300 K in 1140 ps with a nominal cooling rate of 5 K/ps. The temperature was decreased by 0.01 K every time step using a Berendsen thermostat[30] with the time constant parameter for the frictional coefficient set to 0.4 ps. Another 100 ps of equilibration at constant energy and 60 ps at constant pressure ($P = 0$ kbar) using the Berendsen algorithm[30] was performed at 300 K.

The DLPOLY[31] package was employed for MD simulations. Integration of the equation of motion was performed using the Verlet leapfrog algorithm with a time step of 2 fs. Coulombic interactions were calculated by the Ewald summation method[32] with a cutoff of 12 Å and an accuracy of 10^{-4}. The short-range interaction cutoff was set to 6.0 Å.

To determine stress−strain curves, the samples were subjected to uniaxial tensile loading through gradual elongation. Sample deformation was achieved via a stepwise displacement of atoms, $r = (1 + \boldsymbol{\varepsilon})r_0$, where r and r_0 are the displaced and previous positions of an atom at each time step, and $\boldsymbol{\varepsilon}$ is the applied strain. The effect of strain rate on stress−strain diagrams of vitreous silica at 300 K was tested using two strain rates, $\dot{\boldsymbol{\varepsilon}} = 1 \times 10^8$ s^{-1} (SR1) and $\dot{\boldsymbol{\varepsilon}} = 1 \times 10^9$ s^{-1} (SR2). These rates are 2 and 3 orders of magnitude faster than the regime of dynamic or shock loading accessible to experiment.[33] Very fast strain rates are common in simulation work since lower rates require a more difficult computational effort. To our knowledge, SR1 is the slowest strain rate used so far.

Parallelepiped periodic boundary conditions (PBC) were applied along all directions. In previous MD studies, fracture mechanisms were studied, keeping the directions perpendicular to the strained one fixed at the initial value.[6,9−12,15] MD simulations of this type have a null Poisson ratio, and they will be denoted hereafter as constrained simulations (CS). These simulations impose artificial restrictions to the deformation events. Therefore, the code was modified to allow the directions perpendicular to the strained one to relax anisotropically. We refer to these simulations as unconstrained simulations (UCS). They can be easily performed using the Berendsen barostat.[34] Cell vectors and coordinates were scaled by the $\boldsymbol{\eta}$ tensor, which is defined by

$$\eta = 1 - \frac{\beta \Delta t}{\tau_P}(P_{\text{ext}} 1 - \sigma) \tag{1}$$

where β is the isothermal compressibility of the system, Δt is the integrator time step, τ_P is the rise time of the barostat, and P_{ext} is the applied pressure. The component of this tensor along the loading direction is set equal to 1 to keep the direction strained while the others are free to relax. The Berendsen thermostat was applied simultaneously, and four or five iterations were used to obtain convergence.

The components of the stress tensor are calculated by

$$\sigma_{\alpha\beta} = -\frac{1}{V}\left(\sum_i p_{i\alpha} p_{i\beta}/m_i + \sum_i r_{i\alpha} f_{i\beta}\right) \tag{2}$$

where $p_{i\alpha}$, $r_{i\alpha}$, and $f_{i\alpha}$ are, respectively, the α component of the momentum, position, and force acting on the i-th particle with mass m_i. The true stress tensor calculated by eq 2 was transformed into a nominal (or engineering) stress tensor whose normal components are defined by $\boldsymbol{\sigma}_{\text{nom}} = \boldsymbol{\sigma}_t S_i/S_0$, in which S_i and S_0 are the instantaneous and initial cross-sectional area perpendicular to the loading direction. After the stress−strain diagrams were produced, the elastic properties were obtained by direct analysis of curves. All tests were performed at constant temperature and zero external pressure. Thermal effects for silica glass were investigated by performing the simulations at three different temperatures: 100, 300, and 700 K.

Another important property easily obtained by MD simulations is the thermodynamic surface energy γ_t, which is the energy required to create a unit area of surface. It is defined by the relation

$$\gamma_t = \frac{E_b - E_f}{2A} \tag{3}$$

in which E_b, E_f, and A are the bulk energy, the energy after fracture, and the surface area, respectively. However, the thermodynamic surface energy γ_t is different than the fracture surface energy (which is defined as the energy required to create a unit area of surface by fracture) routinely measured by experiments. In fact, the latter is not a function of state, and it depends upon the intermediate processes as plastic deformation and chemical reactions about the tip of the crack. Therefore, the fracture surface energy (γ_f) also was calculated by the relation

$$\gamma_f = \frac{\int_0^{x_f} F \mathrm{d}x}{2A} \tag{4}$$

in which the numerator represents the total work done to fracture the sample. In both cases, the value of the surface area corresponds to a perfectly flat surface neglecting that real surfaces are rough. Hydrostatic compression of the samples at the rate of 5 bar/ps was carried out at 300 K for 20 ps, and the bulk modulus B was obtained according to the thermodynamic formula $B = -V(\mathrm{d}P/\mathrm{d}V)_T$.

The elastic properties (Young's modulus E, shear modulus G, bulk modulus B, and Poisson's ratio ν) of the MD simulated glasses also can be obtained according to the static method, which requires that the energy is minimized using the GULP code.[35] The stiffness matrix elements for a crystalline system are defined as the second derivative of energy U with respect to the strain tensor components.[36] Once the stiffness matrix is obtained, several related mechanical properties of anisotropic materials can be derived from their matrix elements or from the matrix elements of the compliance

(30) Allen, M. P.; Tildesley, D. J. *Computer Simulation of Liquids*; Clarendon Press: Oxford, 1989.
(31) Smith, W.; Forester, T. R. *J. Mol. Graphics* **1996**, *14*, 136.
(32) Ewald, P. P. *Ann. Phys.* **1921**, *64*, 253.
(33) Zhuang, S.; Lu, J.; Ravichandran, G. *J. Appl. Phys. Lett.* **2002**, *80*, 4522.
(34) Berendsen, H. J. C.; Postma, J. P. M.; van Gunsteren, W. F.; DiNola, A.; Haak, J. R. *J. Chem. Phys.* **1984**, *81*, 3684.
(35) Gale, J. D.; Rohl, A. L. *Mol. Simul.* **2003**, *29*, 291.
(36) Ney, J. F. *Physical Properties of Crystals*; Oxford Scientific Publications: Oxford, 1985.

Table 1. Ring Size Distributions of β-Cristobalite and Silica Glass Reported as a Fraction of Ring Numbers in the System

n-fold	2	3	4	5	6	7	8	9	10	11	12
β-cristobalite	0.00	0.00	0.00	0.00	1.00	0.00	0.00	0.00	0.00	0.00	0.00
silica glass	0.00	0.00	0.04	0.14	0.25	0.27	0.17	0.10	0.02	0.01	0.00

matrix. The procedure to calculate elastic properties by using static methods was described fully in previous papers.[28,29]

3. Results and Discussion

The results of structural studies, together with the vibrational density of states (VDOS) and the elastic properties of vitreous silica, obtained by making use of the potential model employed in this work, already were reported in previous papers.[29,37] They will be summarized here for the sake of completing the discussion of the results obtained in this work.

The computed total correlation function $T(r)$ broadened using the method by Wright et al.[6] was shown to match the experimental one reported by Grimley et al.[38] with an R_x factor of 5.5%, and no defect sites or oddly coordinated oxygen and silicon atoms were detected. The calculated Si−Si distance (3.140 Å) was slightly longer with respect to the experimental value (3.077 Å). Si−O and O−O distances of 1.62 and 2.63 Å compared well with experimental data of 1.608 and 2.626 Å as well as an O−Si−O bond angle of 109 ± 7° (109.5 ± 4° from neutron diffraction data). Larger differences were found for the Si−O−Si bond angles, which averaged 152° as compared to NMR data of 146.7°.[39] After constant pressure relaxation at 300 K, the glass showed a slightly higher density (2.26 g/cm^3) with respect to experimental data (2.20 g/cm^3) due to a slight decrease in the Si−O−Si angle.

Table 1 reports the ring size distributions obtained in the present work for both β-cristobalite and silica glass with the latter showing a broad Gaussian shape function centered at the seven-membered rings. We noted previously that the broadening of the ring size distribution in modeled glasses can be overestimated.[37]

3.1. Intrinsic Strength in Amorphous-Cristobalite. Figure 1a shows the stress−strain diagrams for amorphous-cristobalite for the CS ($\nu = 0$) and UCS samples ($\nu \neq 0$) with $\dot{\varepsilon} = 1 \times 10^9$ s^{-1} (SR2), in which the strain was applied along the [001] direction. The diagrams show similar features exhibiting a hardening of the stress−strain ratio with increasing strain. Differences were encountered in the intrinsic strength and strain at failure in the two cases. The system appears to be softer in UCS. The intrinsic strength is $\sigma^* = 27.4$ GPa, and the material fails at a strain of 0.367. On the other hand, in CS, the material breaks at a strain of 0.335 with $\sigma^* = 34.4$ GPa. In both cases, the fracture mechanism is brittle, as expected, and the stress instantaneously drops after the maximum. Because of the translational symmetry of the structure, the interatomic bonds have equal resistance to the applied strain since the atoms are subjected to the same local environments throughout the lattice. At maximum load, the structure fractures catastrophically because of the instantaneous breaking of the Si−O bonds.

Figure 1b shows the average Si−O bond length as a function of strain along the [001] direction. This plot has a very similar shape to the stress−strain diagram with the CS having more strained Si−O bonds. Figure 2a shows changes in the *x*- and *y*-dimensions as a function of the strain along the *z*-direction for UCS. As expected, the changes are equal

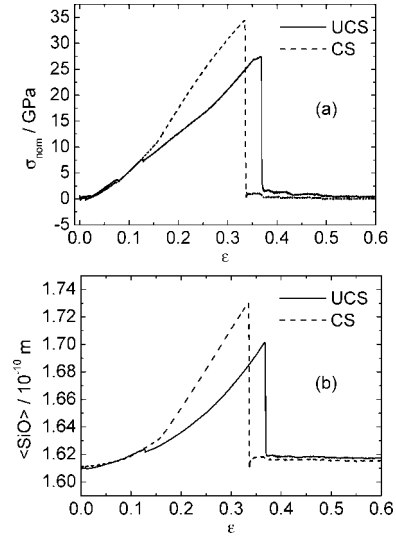

Figure 1. (a) Stress−strain diagrams of amorphous-cristobalite strained along the [001] direction in which the [100] and [010] directions were constrained to initial values (dashed line) or free to relax (solid line). (b) Average Si−O bond length as a function of strain along the *z*-direction.

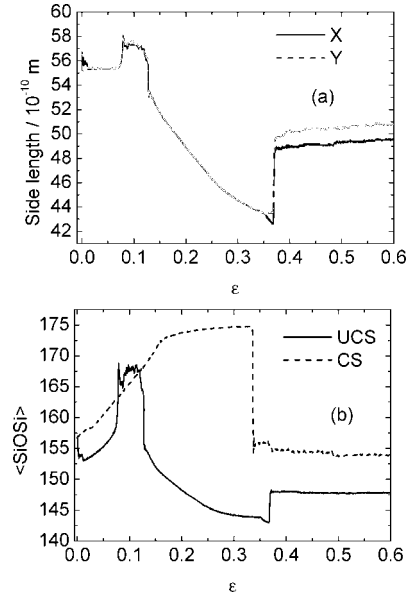

Figure 2. (a) *x*- and *y*-side lengths of amorphous-cristobalite as a function of strain along the *z*-direction and (b) average Si−O−Si bond angle of amorphous-cristobalite as a function of strain along the *z*-direction for constrained (dashed line) and unconstrained (solid line) simulations.

(37) Malavasi, G.; Menziani, M. C.; Pedone, A.; Segre, U. *J. Non-Cryst. Solids* **2006**, *352*, 285.
(38) Grimley, D. I.; Wright, A. C.; Sinclair, R. N. *J. Non-Cryst. Solids* **1990**, *119*, 49.
(39) Clark, T. M.; Grandinetti, P. J.; Florian, P.; Stebbins, J. F. *Phys. Rev. B: Condens. Matter Mater. Phys.* **2004**, *70*, 64202.

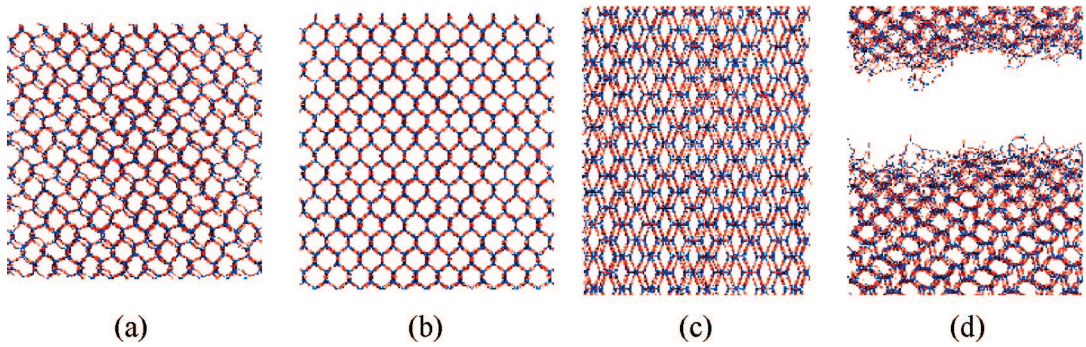

Figure 3. (a) At 300 K, β-cristobalite tends to assume the α-form, but the cubic PBCs do not allow the transition. (b) At 0.1 strain, the structure reassumes the β-form, and the *x*- and *y*-sides expand. (c) At failure strain, the structure is stretched at the stability limit. (d) Structure breaks catastrophically and tends to reassume the α-form. The (110) plane is viewed, and the structures are stretched along the *z*-direction (001).

along both axes, even though the algorithm allows for anisotropic relaxation. An anomalous change is seen for a *z*-strain of up to 0.1. The *x*- and *y*-side lengths show a maximum at 0.1, after which the two lengths decrease until rupture. The same trends were found for the average Si−O−Si angle as a function of *z*-strain. As previously discussed, this anomaly is an artifact due to the starting amorphous-cristobalite configuration. When the strain in the *z*-direction is equal to 10%, all the Si−O−Si angles are reopened at 170−180°, and the structure reassumes the β-form (see Figure 3). Figure 3 also shows that once broken, the material adopts the α-form (because of the temperature of simulation).

In CS, the *x*- and *y*-side lengths are constrained to their initial values, and the change in the average Si−O−Si angle shows a completely different behavior. In fact, the angle opens until rupture of the Si−O bonds. In both cases, the hardening of the stress−strain diagrams after a strain of 0.1 is due to the fact that at lower strains, the applied strain is taken up by Si−O−Si angle opening, with the Si−O bond lengths increasing slowly; subsequently, the strains are taken up by an increase in bond length. Thermodynamic surface energies also are dependent on the PBC constraints; in fact, γ_t for UCS is 3.9 J/m^2 as compared to 2.7 J/m^2 for CS. Similar findings were encountered for the fracture surface energy, with γ_f being 17.0 and 14.1 J/m^2 for the UCS and CS cases.

The previous observations raise the question concerning the behavior of α-cristobalite under tensile tension. Thus, some additional simulations on α-cristobalite were performed. After straining the α-form along the three lattice vectors ([100], [010], and [001]), we observed that the α → β transformation occurred when the unit cell was strained along the [001] direction. Moreover, when strained along the [001] direction, α-crystobalite showed a negative Poisson ratio.

α-Cristobalite is known to be an auxetic material (materials that exhibit negative Poisson ratios) since 1992 when the auxetic behavior for loading in certain directions was independently discovered and reported by Keskar and Chelikowsky[40] who studied this mineral using ab initio

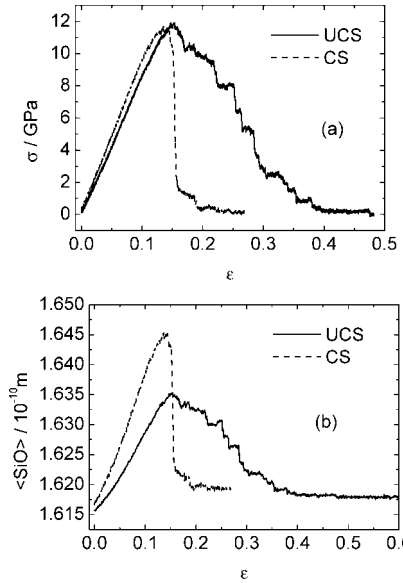

Figure 4. (a) Stress−strain diagram of silica glass for the CS system (dashed line) and UCS one (solid line). (b) Average Si−O bond length as a function of strain.

modeling techniques and Yeganeh-Heeri et al.[41] who measured the single crystalline mechanical properties of α-cristobalite experimentally using brillouin spectroscopy. There have been various attempts to explain this unusual behavior of α-cristobalite.[42–44] We consider that it is very satisfactory that our simulations reproduce this property, but we will not discuss this interesting point further here since it is not the focus of this paper.

3.2. Stress−Strain Diagrams of Silica Glass. Figure 4 shows stress−strain relations of silica glass for the CS and UCS simulations obtained at strain rate of $\dot{\varepsilon} = 1 \times 10^8$ s^{-1} (SR1) and $T = 300$ K. We note that the diagram exhibits all four regions defined previously. Figure 4b shows the average Si−O bond length as a function of strain. As for amorphous-cristobalite, the plot has a similar shape to the stress−strain diagrams. Similar features were found in the average Si−O−Si angle as a function of strain displayed in Fig-

(40) Keskar, N. R.; Chelikowsky, J. R. *Nature (London, U.K.)* **1992**, *358*, 222.
(41) Yeganeh-Haeri, A.; Weiner, D. J.; B, P. J. *Science (Washington, DC, U.S.)* **1992**, *257*, 650.
(42) Alderson, A.; Alderson, K. L.; Evans, K. E.; Grima, J. N.; Williams, J. *Metastable Nanocryst. Mater.* **2005**, *23*, 55.
(43) Alderson, A.; Alderson, K. L.; Evans, K. E.; Grima, J. N.; Williams, M. R.; Davies, P. J. *Phys. Status Solidi B* **2005**, *242*, 499.
(44) Grima, J. N.; Gatt, R.; Alderson, A.; Evans, K. E. *J. Mater. Chem.* **2005**, *15*, 4003.

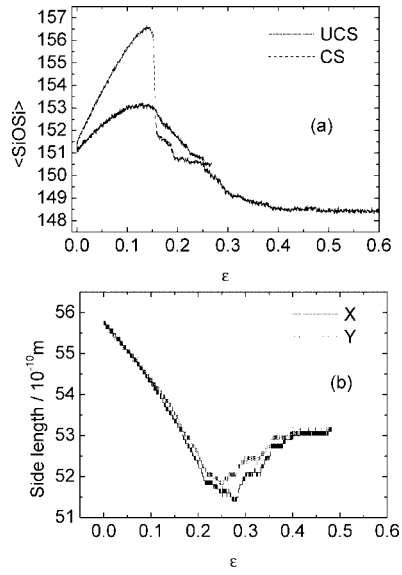

Figure 5. (a) Average Si−O−Si bond angle of silica glass as a function of strain along the *z*-direction for the UCS simulation. After rupture, the Si−O−Si angle drops down to 149° because of the formation of small rings at the surfaces, which have very small bond angles. (b) *x*- and *y*-side lengths of silica glass as a function of strain along the *z*-direction.

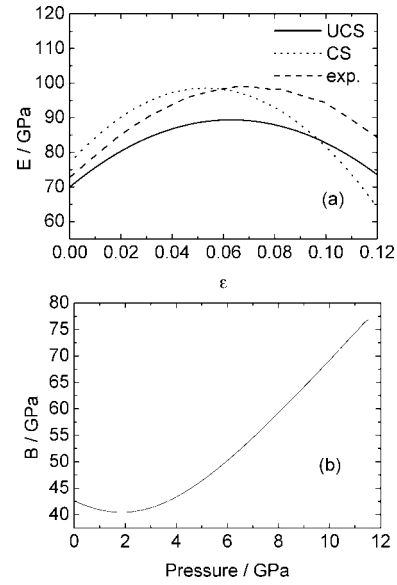

Figure 6. (a) Plot of Young's modulus (GPa) vs strain for UCS (solid line) and CS (dashed line) simulations for silica glass. The dotted line is the best fit obtained by Gupta and Kirkjian[47] with a third-order polynomial to the experimental data of silica fibers.[59] (b) Plot of bulk modulus vs hydrostatic pressure for silica glass at 300 K.

ure 5a. The CS system shows a greater opening of the angle with respect to the UCS. In fact, the maximum value, corresponding to the failure strain in which the material breaks catastrophically, is 157° for CS and 153° for UCS.

Figure 5b shows the *x*- and *y*-box side length variations for silica glass as a function of strain. As expected, the directions perpendicular to the strained direction shrink continuously and isotropically until 0.2 strain; at 0.3 strain, the side lengths stop decreasing and begin to increase as the two new surfaces are formed.

3.2.1. Elastic Region. In the elastic region, the longitudinal stress and longitudinal strain are linearly dependent, and Young's modulus is the proportionality constant. Outside of the elastic region, the nonlinear stress−strain behavior can be described by the following equation where the terms containing powers of strain higher than the third are excluded:[45,46]

$$\sigma(\varepsilon) = E_0\varepsilon + (E_1/2)\varepsilon^2 + (E_2/6)\varepsilon^3 \quad (5)$$

Here, E_0 is the conventional (zero strain) Young's modulus. It is common to define a generalized Young's modulus as the ratio between the stress and the strain also outside of the elastic region. The strain dependence of the generalized Young's modulus is readily obtained by differentiating eq 5

$$E(\varepsilon) = E_0 + E_1\varepsilon + (E_2/2)\varepsilon^2 \quad (6)$$

Figure 6 shows the (nonlinear) behavior of silica glass as a function of strain for the two simulations. The plots were obtained by fitting the initial region of the stress−strain diagrams reported in Figure 4a up to a strain of 12% with a third-order polynomial. In both UCS and CS cases, the fit resulted in an R^2 value of 0.9996 with a standard deviation of 0.60−0.65. The values of the different expansion coefficients are reported in Table 2. Figure 6 also reports the curves obtained by Gupta and Kirkjian[47] by fitting experimental data with a third-order polynomial.

Table 2. Values of E_0, E_1, and E_2 Modulus (GPa) for Silica Glass Calculated from a Third-Order Polynomial Fit (Strain Range of 0−12%) of Stress−Strain Diagram at 300 K and Using SR1[a]

fit params	E_0	E_1	E_2	R^2	SD
exptl[47]	72.3	772	−13058	NR	NR
UCS	69.9	616	−9778	0.9996	0.60
CS	76.9	816	−15379	0.9996	0.65

[a] SD: standard deviation and NR: not reported.

Each plot shows that the Young's modulus increases with strain up to a maximum and then decreases at higher strains. Generally good agreement was found with the experimental data for both CS and UCS. The UCS sample has E_{max} = 89.0 GPa at $\boldsymbol{\varepsilon}_{max} = 0.064$ as compared to 98.8 and 0.07 found by Gupta and Kirkjian.[47] The CS sample shows $E_{max} = 99.0$ GPa at $\boldsymbol{\varepsilon}_{max} = 0.054$. Gupta and Kirkjian[47] fitted the data using Young's modulus at zero strain of 72 GPa, which compares quite well to the values found in our simulations, 69.9 and 76.9 GPa for UCS and CS, respectively.

A detailed analysis of MD trajectories revealed that there is no breaking of Si−O−Si bridges until the maximum in the stress−strain diagram, and as shown in Figure 4b, the stretching of the Si−O bond and, as a consequence, bending of Si−O−Si angles are responsible for the shape of the diagram. Since the results of ab initio calculations show that the Si−O−Si bending constant is negligible,[48,49] the hardening of Young's modulus with strain is likely to be due to the change in the average Si−O bond length with strain, which is dependent on the anharmonic portion of the attractive interatomic potential model.

(45) Mallinder, F. P.; Proctor, B. A. *Phys. Chem. Glasses* **1964**, *5*, 91.
(46) Hiki, Y. *Ann. Rev. Mater. Sci.* **1981**, *11*, 51.
(47) Gupta, P. K.; Kurkjian, C. R. *J. Non-Cryst. Solids* **2005**, *351*, 2324.
(48) Catti, M.; Civalleri, B.; Ugliengo, P. *J. Phys. Chem. B* **2000**, *104*, 7259.
(49) Sierka, M.; Sauer, J. *Faraday Discuss.* **1997**, *106*, 41.

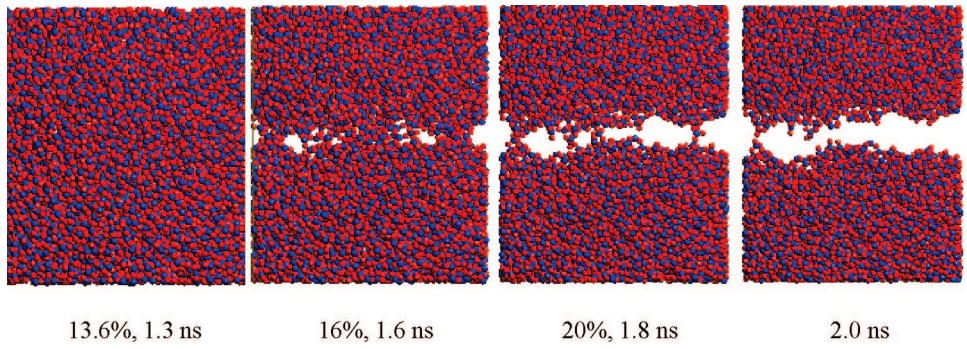

Figure 7. Catastrophic breaking of the CS system.

The observation of a maximum in $E(\varepsilon)$ is in agreement with independent observations of a minimum in the bulk modulus−pressure plot reported in Figure 6b and found experimentally.[50] Huang et al.[51] associated this anomalous mechanical behavior of silica glass with a gradual structural transition similar to the $\alpha-\beta$ phase transition of cristobalite due to the rotation of the Si−O−Si bridge around the Si−Si axis.

3.2.2. Intrinsic Strength. Differences in the stress−strain diagrams were encountered for vitreous silica in CS and UCS samples. In fact, the constrained system has a greater stiffness, higher intrinsic strength ($\sigma^* = 11.7$ GPa), and lower strain at failure ($\varepsilon^* = 13.4\%$) with respect to the unconstrained one, which has $\sigma^* = 10.8$ GPa and $\varepsilon^* = 15.3\%$. These values are in generally good agreement with experimental values at room temperature. In fact, Smith and Michalske[52] measured 11−14 GPa at room temperature and in vacuum ($P = 10^{-8}$ Torr) in tension. Bogatyrjov et al.[53] measured a tin-coated silica fiber at room temperature and found a value of 14.5%, which corresponds to 10.2 GPa using $E = 70$ GPa. Despite the use of the same Si−O interatomic forces for silica glass and amorphous-cristobalite, the latter shows a 3 times greater intrinsic strength with respect to vitreous silica. This is a consequence of the different ring size distribution reported in Table 1. The distribution for vitreous silica is much broader.

3.2.3. Unstable Region. Figure 4 shows that, once the intrinsic strength is reached, the two systems, CS and UCS, behave in different ways. While the CS system clearly breaks catastrophically, the UCS system shows some recovery of the structure. Figures 7 and 8 show the formation and evolution of the crack for the two systems. In the CS system (Figure 7), a sequential breaking of the Si−O bonds occurs and results in the rapid formation of three large voids that coalesce more or less instantaneously to break the material in just 0.2 ns.

Conversely, for the UCS system, there is a gradual breaking of Si−O bonds that can then rearrange through the conformational and topological changes of the rings in the structure. In fact, the shape of the ring size distribution changes during deformation. The sharp Gaussian centered at six- to seven-membered rings becomes broader because of the formation of smaller and larger rings accommodating the voids that grow and coalesce until separation of the material. This phenomenon was observed during 1.4 ns of the simulation and terminated when the strain reached the final value of 0.4. However, from a practical point of view, both 0.2 ns (CS) and 1.4 ns (UCS) time frames are instantaneous, even if the behavior is somewhat different. Therefore, even the UCS system shows a brittle fracture.

The growth of critical voids as a function of strain for the CS and UCS systems was studied. A void can be defined as a region enclosing empty space. In this work, it is assumed that the voids are spherical and that atoms are point particles with no volume so that our results can be compared to the ones reported by Muralidharan et al.[15] The void size distribution was computed using an algorithm, previously developed by us, based on Voronoi−Delanuay tessellation.[37]

Figure 9 shows the radius of the biggest void (BV) as a function of strain for CS and UCS systems. At zero strain, the radius of the BV is ∼3.9 Å. As was shown by Muralidharan et al.,[15] the BV strain curves have three distinct regions, similar to the corresponding stress−strain curves. Region I is characterized by a linear growth in size of the BV that can be related to the elastic deformation of voids because of the enlargement of the Si−O bonds and Si−O−Si bond angles. In region II, the growth stops and the BV size appears to be constant with increasing strain. However, in the CS case, greater fluctuations are present as well as a discontinuity between region I and region II; these are not shown in the UCS case. The fact that the size of the BV does not increase continuously combined with the strain independency of the stress implies that the excess strain is distributed in such a way that only the smaller voids grow via structural rearrangement. Finally, region II is followed in the CS case by a rapid increase in the size of the BV (region III), and once a void with a critical radius (4.7 Å) is formed, then the material breaks instantaneously. On the other side, in the UCS case, the BV increased gradually from 4.4 at ε_{max} to 5.1 at a strain of 0.20, after which it increased rapidly.

From the previous analysis, the values of 4.7 and 5.1 Å for the critical void radius were obtained in the CS and UCS cases, respectively. These values are slightly greater than those reported by Muralidharan et al.,[15] who found a critical void of

(50) Kondo, K.; Iio, S.; Sawaoka, A. *J. Appl. Phys.* **1981**, *52*, 2826.
(51) Huang, L.; Duffrène, L.; Kieffer, J. *J. Non-Cryst. Solids* **2004**, *349*, 1.
(52) Smith, W. A.; Michalske, T. M. DOE Contract DE-AC04-0DPOO789, 1990.
(53) Bogatyrjov, V. A.; Bubnov, M. M.; Dianov, E. M.; Prokhorov, A. M.; Rumyantsev, S. D.; Semjonov, S. L. *JETP Lett. (Engl. Transl.)* **1988**, *14*, 383.

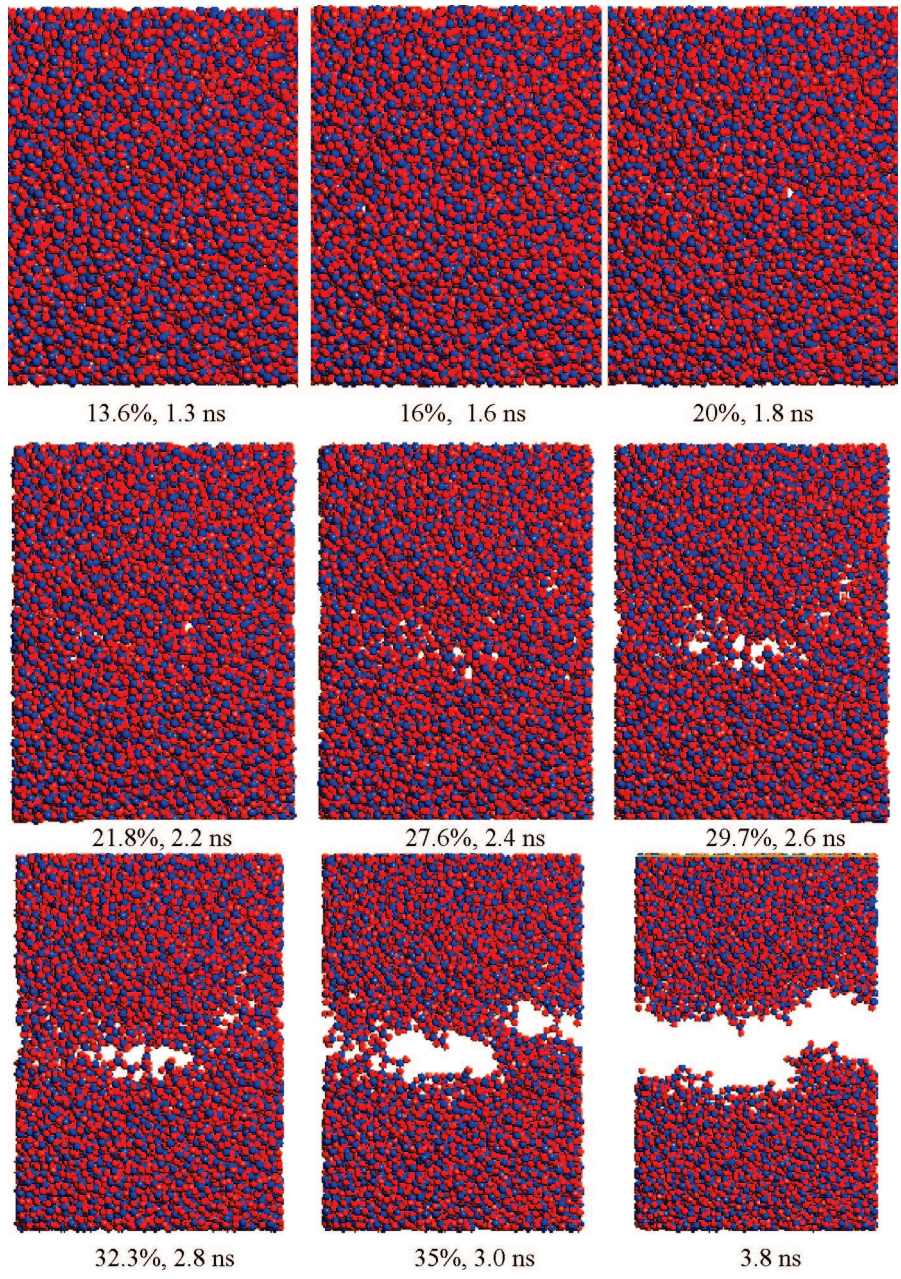

Figure 8. Formation and evolution of crack for the UCS simulation, nanoseconds of MD trajectory, and percent strain are reported. Micropores developed, and they coalesced to release the stress.

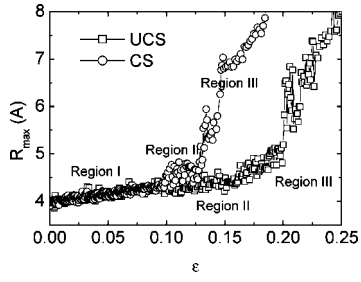

Figure 9. Growth of critical void as a function of strain for CS and UCS simulations carried out at 300 K with a strain rate of 1×10^8 s^{-1}.

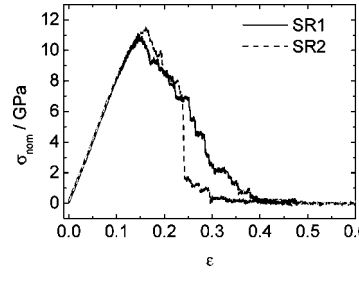

Figure 10. Stress−strain behavior of the UCS system at different strain rates and $T = 300$ K.

4.0 Å for a strain rate of 5×10^9 s^{-1} but with smaller simulation boxes containing ~3000 atoms. However, our results are still not comparable to the cavities that are 20 nm long and 5 nm deep reported by Célarié et al.[26] because of the relatively small box size used in our simulations (5.6 nm).

The combination of void size analysis and graphical inspection of the trajectory during the stress−strain experiment simulation allows us to explain the microscopic events shown in Figures 4a and 5b). In the region around the maximum stress (between $\varepsilon = 0.15$ and $\varepsilon = 0.2$), the small

Table 3. Mechanical Properties Extrapolated from Stress−Strain Diagrams of Silica Glass When Perpendicular Direction of Tensile Stress Is Kept Fixed and Free to Relax[a]

	constrained				unconstrained			
T (K)	100	300	700	300	100	300	700	300
$\dot{\varepsilon}$	10^9/s	10^9/s	10^9/s	10^8/s	10^9/s	10^9/s	10^9/s	10^8/s
E_0 (GPa)	79.1 ± 0.3	78.0 ± 0.7	76.6 ± 1.0	76.9 ± 0.8	72.8 ± 0.3	69.4 ± 0.8	64.0 ± 0.8	69.9 ± 0.5
$E_{max}/\varepsilon_{max}$	102.4/0.060	100.5/0.054	96.3/0.049	99.0/0.053	95.2/0.094	91.1/0.064	91.5/0.059	89.0/0.064
σ^* (GPa)	13.0	12.3	10.9	11.7	12.2	11.4	9.7	10.8
ε^*	0.152	0.144	0.139	0.134	0.166	0.164	0.143	0.153
γ_t (J/m^2)	1.6	1.6	1.5	1.6	2.1	2.1	3.8	2.5
γ_f (J/m^2)	3.8	3.6	3.3	3.2	5.3	5.5		6.5

[a] E_0 is Young's modulus at zero strain, E_{max} is the maximum of the E/strain diagrams, and ε_{max} is the strain at maximum E. σ^* and ε^* are intrinsic fracture strength and strain, respectively, while γ_t is the thermodynamic surface energy and γ_f is the fracture surface energy.

voids are disposed far from one another; at $\varepsilon = 0.2$, they finally coalesce to voids with a critical radius, which expands until $\varepsilon = 0.3$. At this value, the discontinuity occurs in the x- and y-variations as a function of strain (Figure 4b). For strain values greater than $\varepsilon = 0.3$, the glass can be considered to be already broken, and the x- and y-side lengths re-expand until separation is complete.

3.2.4. Effect of Strain Rate on Stress−Strain Diagrams of Silica Glass. Figure 10 shows the dependence of the stress−strain diagrams as a function of strain rate at $T =$ 300 K. As found by Muralidharan et al.,[15] the intrinsic strength and strain at failure increased with increasing strain rate both for CS (not shown here) and UCS samples, while the elastic region seems to be independent of strain rate. This is probably due to the rather low values of the strain rate we used, in the range of 10^8 to $\sim 10^9$ s^{-1}. In fact, Simmons et al.,[6,9–12,15] using a faster strain rate between 5×10^{10} and 5×10^{12} s^{-1}, found that the elastic region appeared to be independent of strain rate only for the lower strain rates. At higher strain rates, the modulus appeared to increase with strain rate. They also observed that a different mechanism of fracture occurred for different strain rates. At very high strain rates, the applied strain was taken up by the increase in bond lengths, while for low strain rates, the strain was first related to the increase of bond angles and subsequently to the increase in bond lengths.

The dependence of the intrinsic strengths, the strains at failure, and the fracture energies for both CS and UCS samples as a function of strain rates are reported in Table 3. These results agree quite well with experimental findings, which show that the strength in brittle materials increases by increasing the strain rate.[54]

For the CS case, the thermodynamic surface energy calculated according to eq 3 is independent of the strain rate as well as temperature. Conversely, for the UCS case, the thermodynamic surface energy is dependent on both strain rate and temperature. Thermodynamic surface energy γ_t increases with decreasing strain rates and increasing temperature. Table 3 shows that fracture surface energy calculated according to eq 4 is strain rate and temperature dependent, in both cases. In fact, for the UCS system, γ_f increases with decreasing strain rate and increasing temperature, while for the CS system, it shows an opposite trend.

Experimentally, fracture surface energies of vitreous silica range from 3.70 to 5.0 J/m^2 according to the test method employed.[55] These values are quite different from those found in our study because of several factors: different environments (i.e., vacuum in MD simulations and moisture in experiments), different values of strain rates that are much lower in the real word, intrinsic limitations of computer simulations, such as the use of periodic boundary conditions with a small number of atoms, and, here, the lack of external surfaces in the staring configurations. Although the absolute values of thermodynamic fracture surface energy calculated by computer simulations are not comparable to the experimental fracture surface energy, preliminary simulations of soda-lime glasses that are currently in progress in our laboratories have shown that the relative trends with different compositions are well-reproduced.

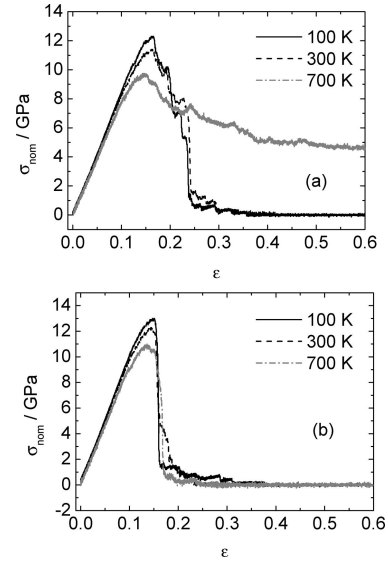

Figure 11. (a) Stress−strain behavior of silica glass at different temperatures for the UCS system. (b) Stress−strain behavior of silica glass at different temperatures for the CS system.

3.2.5. Effect of Temperature on Stress−Strain Diagrams of Silica Glass. Table 3 and Figure 11 show how the stress−strain diagrams of UCS and CS systems are affected by temperature changes. At 100 K, the strength of silica glass increases to 12.2 GPa with a failure strain of 16.3% for the UCS system, while in the case of the CS system, the intrinsic strength increases to 13 GPa with a failure strain of 15.2%. These are in generally good agreement with inert intrinsic

(54) Pollock, J. T. A.; Hurley, G. F. *J. Mater. Sci.* **1973**, *8*, 1595.

(55) Lucas, J. P.; Moody, N. R.; Robinson, S. L.; Hanrock, J.; Hwang, R. Q. *Scripta Metall. Mater.* **1995**, 743.

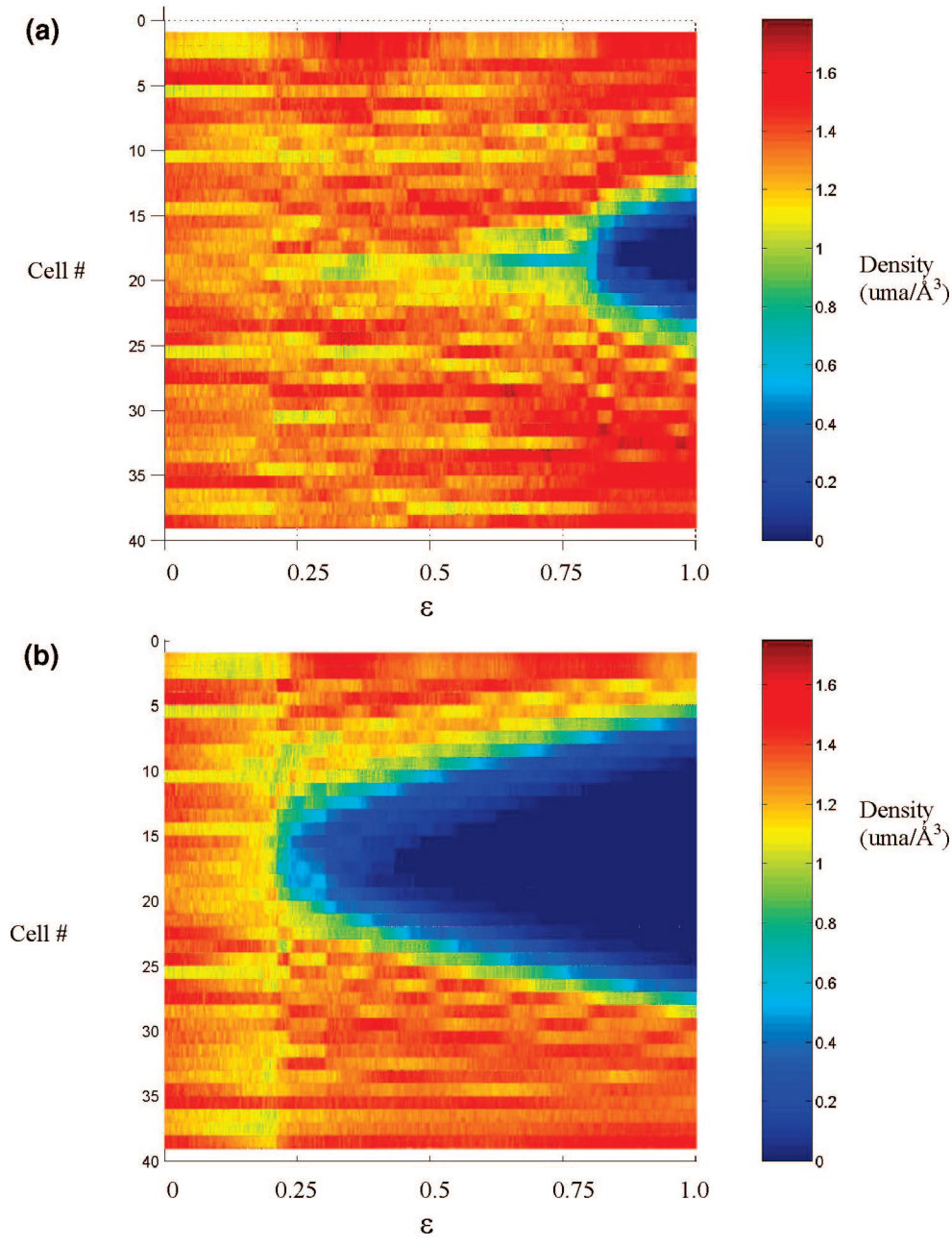

Figure 12. Density fluctuation along strained direction (y) vs strain (x) for (a) UCS system and (b) CS system at 700 K.

strength measured experimentally. In fact, Proctor et al.[56] measured 12−13 GPa at 77 K but 14 GPa at 4 K in tension. France et al.[57] measured a two-point bend strain of 18% at 77 K.

It is clear that both intrinsic strength and Young's modulus decrease as the temperature increases. At 700 K, there is more plastic deformation in the case of the UCS system, with respect to the CS system. The stress−strain curve follows the elastic curve up to the yield point, and after the maximum, the applied stress becomes constant, independent of strain. However, this region is associated with the constancy of the average Si−O bond length because of the recovery allowed by density fluctuations and the rearrangement of rings with different sizes present in the glass. To study density fluctuations, the box was divided into 40 raw cells along the strained direction, and the density inside the cells was calculated as a function of strain (Figure 12). The material density is not homogeneous along the strained direction and varies discontinuously as a function of time, and localized density fluctuations are shown until fracture occurs. The heterogeneous density is related to the heterogeneous ring size distributions in glasses. The same plastic behavior is observed at 300 K for smaller UCS systems of ∼3000 atoms. This observation suggests a size dependency of the stress−strain diagrams that is not observed in the CS case. Several tests should be performed with much larger systems (hundreds of thousands of atoms) to check if this size dependency occurs in the case of the UCS system.

(56) Proctor, B. A.; Whitney, I.; Johnson, J. W. *Proc. R. Soc. London, Ser. A* **1967**, *297*, 534.

(57) France, P. W.; Duncan, W. J.; Smith, D. G.; Beales, K. J. *J. Mater. Sci.* **1983**, *18*, 126.

Table 4. Elastic Properties Extrapolated from Stress−Strain Diagrams as Compared to Properties Calculated by Static Methods (MM-GULP) and Experimental Methods[58]

			unconstrained MD		
	exptl	MM-GULP	100 K	300 K	700 K
E (GPa)	72.50	70.90	72.8	69.9	64.0
G (GPa)[a]	31.25	29.60	28.3	27.4	25.4
B (GPa)	36.10	36.40	44.2	42.5	41.6
ν	0.160	0.175	0.286	0.277	0.260

[a] Shear modulus was calculated using the relation $G = E/\{2(1 + \nu)\}$, in which E and ν were extrapolated from the stress−strain diagrams.

However, these calculations are outside the realm of our computer resources at the moment and will be considered in the future.

As expected, the elastic properties decrease with increasing the temperature, leading to softening of the material (see Table 4).

3.2.6. Elastic Properties: Strained MD Simulations versus Static Methods. Table 4 reports the values of elastic properties E, G, B, and ν for silica glass, extrapolated from the stress−strain diagrams of the UCS system with a strain rate of 10^9/s, as compared to values calculated by means of static methods,[28] as well as to experimental data. The results obtained by means of static methods (MM-GULP) show better agreement with experimental data, with typical errors of 2, 5, 1, and 9% for E, G, B, and ν, respectively. This is probably due to the fact that the potential parameters used here were fitted to the structure and mechanical properties of α-quartz using the static method[28] and do not include temperature effects. On the other hand, the results obtained from MD simulations reveal that while Young's modulus is in generally good agreement, bulk modulus and Poisson's ratio are rather overestimated, probably because elastic properties obtained from MD simulations explicitly include thermal effects and kinetic energy. Moreover, the two methods employ slightly different equations. Therefore, the fact that the elastic properties extrapolated from stress−strain diagrams show larger differences as compared to the experimental data does not imply that the dynamic method is worse than the static one; extrapolating from stress−strain curves is an inherently less accurate approach. We note that, as expected, the elastic properties decrease with increasing temperature, leading to material softening.

4. Conclusion

The stress−strain behavior of crystalline and vitreous silica was studied under different loading conditions. A completely brittle fracture mechanism was observed for crystalline silica both in the CS and in the UCS cases. However, different mechanisms occurred during rupture of vitreous silica depending on the constraints applied along the transverse directions. The imposition of a null Poisson's ratio led to a brittle fracture in which the formation of voids and their coalescence occurred in ∼0.2 ns.

When the x- and y-dimensions are free to relax during tensile loading along the z-direction, the growth and coalescence of the small voids are more pronounced. However, because of the limited box dimensions, the critical voids that led to the fracture were smaller than those observed experimentally.[26] Further simulations with 10^8-10^{10} atoms should be carried out since the cavities that were found are at least 1 order of magnitude larger than the voids detected in our simulations.

A negative Poisson's ratio was found for α-crystobalite due to the $\alpha \rightarrow \beta$ phase transformation occurring when the material was strained along the [001] direction. The intrinsic strength of crystalline silica as compared to vitreous silica highlights the paramount importance of ring size distribution on the mechanical properties of the final material. The anomalous behavior of silica glass as well as the effects of temperature and strain rate on the stress−strain diagrams were well-reproduced. Their behavior was found to be in agreement with general experimental knowledge.

Acknowledgment. This work was supported by the Ministero dell'Istruzione, Università e Ricerca (MIUR, Grant 2003032158_005). A.P. acknowledges financial support for his visit at Alfred University provided by the International Materials Institute for New Functionality in Glass (Grant DMR-0409588), Lehigh University, Bethlehem, PA.

CM800413V

(58) Lucas, J. P.; Moody, N. R.; Robinson, S. L.; Hanrock, J.; Hwang, R. Q. *Scripta Metall. Mater.* **1995**, 743.
(59) Krause, J. T.; Testardi, L. R.; Thurston, R. N. *Phys. Chem. Glasses* **1979**, *20*, 135.